System identification and artificial intelligent (AI) modelling of the molten salt electrolysis process for prediction of the anode effect

Ozan Kaya [a,b], Masoud Abedinifar [a], Dominic Feldhaus [b], Fabian Diaz [b,*], Şeniz Ertuğrul [c], Bernd Friedrich [b]

[a] Department of Mechatronics Engineering, Istanbul Technical University, Istanbul 34467, Turkey
[b] IME Process Metallurgy and Metal Recycling, RWTH Aachen University, Aachen 52072, Germany
[c] Department of Mechatronics Engineering, Izmir University of Economics, Izmir 35330, Turkey

A R T I C L E   I N F O

A B S T R A C T

NdFeB magnets are widely used in various applications including electric and hybrid vehicles, wind turbines, and computer hard drives. They contain approximately 31–32 wt% Rare Earth Elements (REEs), mainly neodymium (Nd) and praseodymium (Pr), and are produced by molten salt electrolysis using fluoride electrolytes. However, anode passivation or anode effect may occur, generating greenhouse gases if insufficient amounts of metal oxides are available in the system. Therefore, in this study, a dynamic model of the electrochemical process was developed to estimate the system variables and predict the anode effect using several system identification methods. The Transfer Function (TF) estimation, Auto-Regressive with Extra inputs (ARX), Hammerstein-Weiner (HW), and Artificial Neural Network (ANN) models were used, and their results were compared based on the occurrence of the anode effect. The best model achieved an average accuracy of 96% in predicting the process output.

1. Introduction

Over the past few years, high-tech NdFeB magnets have gained increasing popularity in electric and hybrid vehicles, wind turbines, and computer hard drives [1,2]. These magnets typically contain approximately 31–32 wt% Rare Earth Elements (REEs), mainly neodymium (Nd) and praseodymium (Pr), depending on their application. Nd and Pr are produced through molten-salt electrolysis, an energy-intensive production method in which metal oxides are added to the molten salt. These oxides split into oxygen and metal ions, which then react at the electrodes to form gases and metals via the addition of electrical energy. The molten salt, which is electrically conductive, served as an electrolyte. Chloride-, fluoride-, alkali oxide-, and alkaline earth metal-based electrolytes have been previously investigated for this purpose [3–5]. Among these, fluoride electrolytes are the most suitable for Nd/Pr deposition because they offer high conductivity, low hygroscopy, and high current efficiency compared to chloride electrolytes [6,7]. Commonly used fluoride electrolytes include LiF (NaF or KF) and CaF$_2$, with LiF being used alongside neodymium fluoride (NdF$_3$) and praseodymium fluoride (PrF$_3$) in most studies because of its positive influence

on the electrical conductivity, fluidity, and oxide solubility of the electrolyte [4–12].

This technology operates as a semi-continuous process, with the input material periodically charged during operation. If insufficient metal oxides are available in the system, the fluorides of the electrolyte participate in the electrochemical reaction at the anode, leading to the formation of CxFy gases instead of COx. Perfluorocarbon (PFC) gases have a CO2 equivalent of 7000–12000, raising environmental concerns [13]. Such conditions are usually referred to as anode passivation or anode effect. Thus, feeding the system with sufficient oxides during Molten Salt Electrolysis is critical for preventing system instability and the generation of greenhouse gases.

For this purpose, appropriate models related to the output behaviour of the process are required to estimate the system variables. Even if the system has a chaotic response caused by uncertainty or nonlinearity, the most straightforward modelling approaches, such as linear models, provide information regarding system order, number of phases, and frequency differences. As these linear models consist of simple dynamic relations, they can be useful in terms of easy implementation once satisfactory models are obtained. In this method, to define the system

---

order, response analysis methods such as impulse or step response can be executed analytically using a dynamic dataset. In [14], the groundwater system was examined using its step response to identify the properties that determine the dynamics of a groundwater system. The orders of the Molten Salt Electrolysis process, such as those of the Impulse Response (IR), can be computed using step-response analysis. In this case, the use of ratio response analysis orders facilitates the determination of the Transfer Function (TF) coefficients. Generally, TF models are extensively used to demonstrate models of systems that exhibit linear dynamical behaviour [15]. In [16–17], the TF model was used to identify the behaviour of real-world processes. Furthermore, the TF model is used to characterise a process that exhibits highly unstable dynamical behaviour [18]. However, in many cases, TF models may be insufficient if a high accuracy is required.

When a linear model is used, an autoregressive model with extra inputs (ARX) can be used to increase the accuracy of the linear model [19]. In this approach, additional inputs are included in the linear model to minimise the estimation error by performing a numerical analysis with least-squares estimation (LSE). In [20–21], different approaches were proposed for identifying hybrid and unforeseen dynamic processes using ARX. Although the ARX model has been successfully applied in the literature, in practice, it can be relatively inefficient or result in low accuracy in nonlinear systems. Therefore, for processes that exhibit high nonlinearity, linearisation or nonlinear models may be required to achieve accurate system behaviour. In contrast, the Hammerstein-Wiener (HW) models are commonly used to model highly nonlinear systems [22]. These models are extensively used to represent the mathematical models of systems, using one or two static nonlinear models in series with a linear model. In [23–24], HW models were suggested to achieve high fitting performance for processes with nonlinear behaviour. Nevertheless, nonlinear system models are complex solutions that may not fulfil the requirements to overcome real-time implementations [25].

Artificial Neural Networks (ANN) are another approach frequently used for modelling and process identification [26,27]. Moreover, an ANN functions as an artificial process model based on the black box approach [28]. In [29,30], an ANN was not only implemented to enhance the response of the dynamic model of a standard chemical process, but was also used for identifying chemical reactions. Furthermore, ANN can be used to improve the process efficiency [31] or predict undesirable events during operation [32].

In the Molten Salt Electrolysis, passivation of the anode or the anode effect corresponds to an undesired event in the extractive method. Once the Anode effect occurs in the cell, the dynamic parameters of the process vary over time. Some of these parameters include the feeding of the materials, off-gas composition, temperature, voltage, and current. These measured variables can be used to generate models using different methods such as TF, ARX, HW, and ANN. In practice, normal process behaviour without an anode effect corresponds to a low-frequency and stable process. However, it can suddenly change to a high-frequency response once the Anode Effect occurs.

In this study, different system identification models (TF, ARX, HW, and ANN) were used based on the recorded process variables to evaluate their performance and identify the occurrence of the anode effect during Nd and Pr production. In addition, the general process description of Molten Salt Electrolysis, data acquisition strategy, data preparation, and modelling strategy are addressed in detail.

2. Material and methods

2.1. Molten salt electrolysis process

The used electrolyte consists of 61.3 wt% neodymium fluoride (NdF3, Treibacher, Althofen, Austria, $\geq$ 99.5 %), 26,2 wt%

praseodymium fluoride (PrF3, Treibacher, Althofen, Austria, $\geq$ 99.5 %) and 12.5 wt% lithium fluoride (LiF, Treibacher, Althofen, Austria, $\geq$ 99.5 %). This composition was selected on the basis of previous tests [33,34].

The electrolyte was melted at approximately 1100 °C in advance to prepare it for Molten Salt Electrolysis. The components were predried at 200 °C for 24 h, mixed, and placed in a graphite crucible. They were then heated in an induction furnace until they reached the desired temperature (1100 °C) and the mixture became a liquid. The atmosphere for this material preparation was a 2 bar Ar overpressure. The conditions listed above were used to prevent evaporation of the component with the lowest vapour pressure, such as lithium fluoride. When the powder was molten, the liquid electrolyte was cast into a high-purity graphite mould and allowed to solidify.

The premolten electrolyte was homogenised using the method described above. Consequently, the produced material had a much higher density than the initial powders; otherwise, the materials would not fit inside the crucible during the electrolysis. Next to the electrolyte, the oxides used for electrolysis, neodymium oxide (Nd$_2$O$_3$, Treibacher, Althofen, Austria, $\geq$ 99 %) and praseodymium oxide (Pr$_6$O$_{11}$, Treibacher, Althofen, Austria, $\geq$ 99 %), were dried at 200 °C for 24 h. These oxides were then mixed in a composition of 70 % Nd$_2$O$_3$ and 30 % Pr$_6$O$_{11}$, and pressed into pellets at 100 N. Finally, the pellets were crushed to obtain grain sizes between 60 and 200 μm. This step is necessary to ensure the feeding properties of the powder, which would otherwise clump and cause clogging.

The Molten Salt Electrolysis was conducted in a gas-tight steel cell with a water-cooled lid (Fig. 1). This part must be cooled, as rubber seals are used to ensure the tightness of the system. The electrodes used for electrolysis were a high-purity graphite ring anode to provide the maximum active surface and a molybdenum cathode. Both were inserted into the cell using the Swagelok system. This has the advantage that the immersion depth can be varied without gas escaping. Next to the electrodes, the lid had holes for the thermocouple and gas measurement system (Fourier transform infrared spectroscopy, FTIR-Gasmet DX4000, Germany). Finally, the crucible, filled with electrolyte, was placed in a steel cylinder, as shown in Fig. 1, before the lid was attached and the reactor was sealed.

The prepared oxides were stored in a feeding system cylinder that could also be sealed. At the feeding command, the screw in the feeding device rotated, carrying oxide grains from the cylinder into the cell. The feeding system was placed on a high-precision balance to record the amount of oxide fed into a crucible. The aim is to feed the oxides at 2 wt % of the electrolyte to avoid exceeding the maximum solubility, which is between 3 and 4 wt% [35–37].

After preparation, the cell was placed in a resistance-heated furnace that heated the system to 1050 °C. When the electrolyte was molten, the electrodes were immersed and the wires were connected to a Munk rectifier (maximum 30 V, 200 A). Under normal conditions, the target current is set to 30 mA.

The off-gas analysis system extracted the gas directly from the cell at a constant rate of 3 l/min. The gas was sampled for 5 s and analysed during this interval. The cell voltage and supplied current, which were continuously recorded throughout the process, were monitored.

When Nd$_2$O$_3$ and Pr$_6$O$_{11}$ were fed into the system, they melted and dissolved. They form complexes with fluoride electrolytes called oxyfluorides, which then react electrochemically at the electrode surfaces (anode and cathode).

For neodymium, the complex formation [40] is shown in Eq. (1).

$$\text{Nd}_2\text{O}_3 + [\text{NdF}_6]^{3-} + 9\text{F}^- = 3[\text{NdOF}_5]^{4-} \tag{1}$$
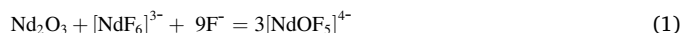
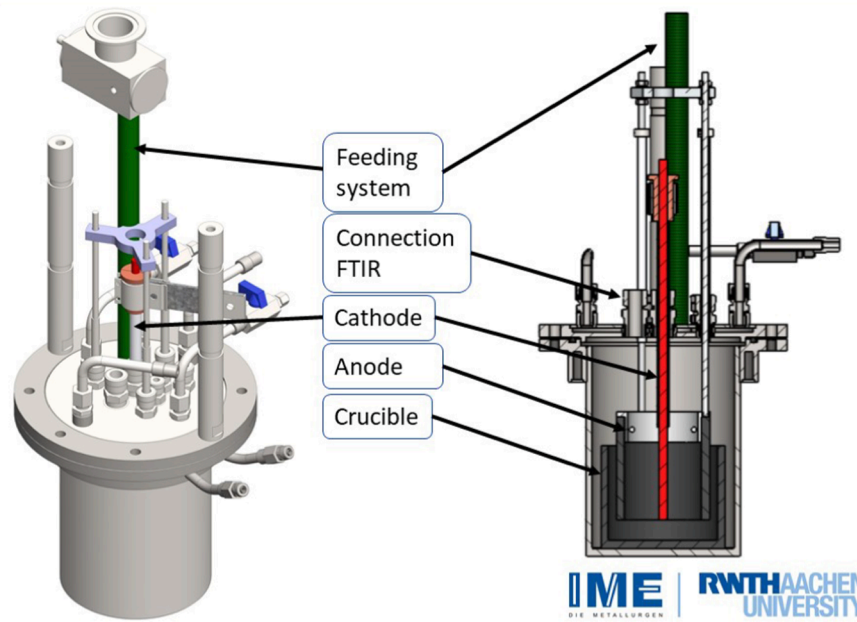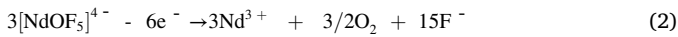When the decomposition potential is reached, these oxyfluorides [40] react further, as shown in Eq. (2):

Fig. 1. The experimental setup of the Molten Salt Electrolysis includes a feeding system, Connection FTIR, Cathode, Anode, and Crucible.

$$3[NdOF_5]^{4-} - 6e^- \rightarrow 3Nd^{3+} + 3/2O_2 + 15F^- \tag{2}$$

The Nd ions were then electrochemically reduced to metallic Nd(0) at the cathode [40] in two steps, using Eq. (3) and (4):

$$\text{Step 1}: \quad Nd^{3+} + e^- \rightarrow Nd^{2+} \tag{3}$$

$$\text{Step 2}: \quad Nd^{2+} + 2e^- \rightarrow Nd(0) \tag{4}$$

As praseodymium and neodymium are chemically similar, it is assumed that the complex formation of praseodymium ions proceeds similarly. However, studies have revealed [39] that praseodymium is not deposited on the cathode in two steps, but in only one step, using Eq. (5).

$$\text{Step 1}: \quad Pr^{3+} + 3e^- \rightarrow Pr(0) \tag{5}$$

Neodymium and praseodymium are deposited on the cathode. The metal collected in the liquid form on the electrode surface drops owing to its high melting temperature and density difference. The metal produced was then collected in a molybdenum crucible located directly under the cathode at the end of the process. In addition, the Mo crucible was removed after the experiment to determine the metal yield and product quality.

While metal ions are deposited at the cathode, oxygen is formed at the anode from its ions and reacts with the carbon of the electrode to form CO or CO_2 gas. These gas bubbles easily detach from the anode and rise, which leads to the natural convection of the electrolyte and transports new ions to the electrons. Under certain conditions, the lack of oxides results in insufficient ions at the electrodes. Thus, the cell potential increased, leading to different electrochemical reactions [40].

Most probably, intermediate products, such as COF and COF_2, are also formed during electrolysis, but these are not stable and react further with PFCs [38]. Consequently, research was conducted to investigate the effect of the potential on off-gas production to evaluate the process conditions. These results agree with the assertion that CO and CO_2 are typically formed during the process and that CF_4 and C_2F_6 might be generated only at higher cell potentials, as shown in Fig. 2.

Compared with CO/CO_2, PFC gases have a much higher wettability to the electrodes [37], which means that the formed PFC bubbles adhere to the electrode. Under these conditions, each bubble on the surface of the electrodes inactivates the surface by a fraction that prevents the
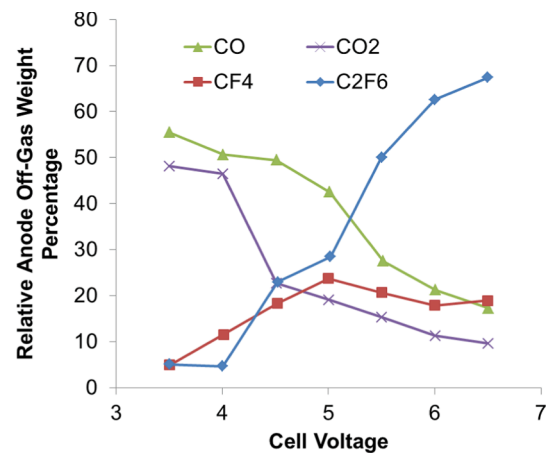

Fig. 2. Gas formation over the cell potential in neodymium electrolysis [41].

current from flowing through the cell. Consequently, the surface passivated by the PFC gas bubble θ was subtracted from the active surface of electrode A. In addition, the cell current was kept constant, and the current density, j, increased with each bubble that adhered to the electrode surface, as shown in Eq. (6).

$$j = \frac{I}{A(1-\theta)} \tag{6}$$

The formation of a gaseous film on the electrode depends on the wettability of the melt or gas on the surface of the electrode, which in turn depends on different parameters such as the electrolyte temperature, metal oxide content, electrode shape, and surface texture [37].

If the current density increases, the reaction rate also increases, resulting in the formation of more PFC gases that adhere to the surface. This effect rises exponentially until the electrode is completely covered by bubbles. The current flow stops at this moment and the currency value is nearly zero, whereas the cell potential increases significantly. In this state, the process is stopped and no metal can be produced until fresh oxides are fed into the system. Even then, it takes some time for PFC gases to leave the system. In addition to environmental issues, this represents a significant energy cost because the system must remain

molten at ~ 1200 °C when no metal is produced. Therefore, identifying, predicting, and avoiding node effects is essential for maintaining the stability and efficiency of the system.

2.2. Experimental data

Several conditions on the boundaries of the inputs were applied to create a proper model and examine the relationship between the input and output parameters. The temperature was set to 1200 °C for each experiment and the current was set stepwise at different levels in each experiment. Notably, the current dropped to zero when the anode effect occurred and the feeding material was supplied at a rate of 20 g each time the anode effect occurred in the cell. The general stepwise strategy (input data) for data collection is illustrated in Fig. 3.

As a result of the experiments, the gathered output data were divided into training and evaluation data to develop and validate both the dynamic models and the artificial neural network model of the Molten Salt Electrolysis process. Finally, all evaluated models considered in this study were compared.

3. Theory and calculation

3.1. System identification models

After collecting the output datasets (CO, CF_4, CO_2, and Voltage), the model identification methods were used to characterise the system response. Step response is used to define the frequency, system order, and number of phases. In this study, the complexity of the identification methods was derived from a simple linear method to a nonlinear method. First, the TF model is applied as a linear model. Subsequently, a linear ARX model was developed. Finally, the HW method was built as a nonlinear model owing to the nonlinearity of the Molten Salt Electrolysis.

3.1.1. Transfer function estimation model

Transfer Function (TF) estimation as a linear model of the Molten Salt Electrolysis process is utilised because it is easily implemented to estimate the future output of the system. For this purpose, a step-response analysis was conducted to investigate the relationships between system inputs and outputs. A graphical structure of the step-response analysis is shown in Fig. 4.

As a result, all orders of the TFs were defined. The highest order of TFs was set to 2. The generalised TF is given by Eq. (7).

$$TF = G_{ij} = e^{((d_1 * s))} * \frac{a_1 s^2 + a_2 s + a_3}{b_1 s^2 + b_2 s + b_3} \tag{7}$$

where i represents the number of control inputs, j is the number of outputs, d_1 is the time delay between the input and outputs, $a_k (k = 1, 2, 3)$ is the coefficient of the zero polynomial of TF, and $b_k (k = 1, 2, 3)$ is the coefficient of the pole polynomial of TF. Using Eq. (7), the output relations for each parameter are generated, as shown in Eq. (8).

$$y_j = \sum_{i=1}^{2} (U_i * G_{ij}) \tag{8}$$

where y represents the output parameters and U is a control parameter.

All coefficients of the TFs were defined using a Sequential Quadratic Programming (SQP) optimiser utilising the training dataset. The obtained transfer functions corresponding to the outputs, including the Voltage, CO, CO_2, and CF_4, to the current input and feeding input, are given in Eq. 9-12 and Eq. 13-16, respectively.

$$G_{CO,Current} = \frac{CO}{Current} = \frac{573.5s^2 + 60.33s - 0.00617}{s^2 + 0.0338s + (8.55 \times 10^{-6})} \tag{9}$$

$$G_{CO_2,Current} = \frac{CO_2}{Current} = e^{(-8s)} \frac{-0.01374s^2 + 3.09 \times 10^{-6}s - 9.005 \times 10^{-7}}{s^2 + 0.001134s + 0.000113} \tag{10}$$

$$G_{CF_4,Current} = \frac{CF_4}{Current} = e^{(-3s)} \frac{-0.00691s^2 - 0.00954s + 3.552 \times 10^{-6}}{s^2 + 0.03801s + 3.728 \times 10^{-5}} \tag{11}$$

$$G_{Voltage,Current} = \frac{Voltage}{Current} = e^{(-10s)} \frac{-0.174s^2 + 0.002299s + 4.584 \times 10^{-7}}{s^2 + 0.03799s + (3.536 \times 10^{-5})} \tag{12}$$

$$G_{CO,Feeding} = \frac{CO}{Feeding} = e^{(-12s)} \frac{17.43s + 0.02682}{s^2 + 0.0002227s + (1.656 \times 10^{-7})} \tag{13}$$

$$G_{CO_2,Feeding} = \frac{CO_2}{Feeding} = e^{(-2s)} \frac{0.006607s + 4.621 \times 10^{-6}}{s^2 + 0.007624s + 1.341 \times 10^{-6}} \tag{14}$$

$$G_{CF_4,Feeding} = \frac{CF_4}{Feeding} = e^{(-s)} \frac{0.02063s - 8.216 \times 10^{-5}}{s^2 + 0.009264s + 1.329 \times 10^{-6}} \tag{15}$$

$$G_{Voltage,Feeding} = \frac{Voltage}{Feeding} = e^{(-s)} \frac{0.1475s^2 - 0.04194s + 0.005095}{s^2 + 0.04253s + 0.002336} \tag{16}$$

As seen in Eq. 9-16, the order of the transfer functions, including $G_{CO,Feeding}$, $G_{CO_2,Feeding}$ and $G_{CF_4,Feeding}$, is equal to 1. The order of the rest of the transfer functions ($G_{CO,Current}$, $G_{CO_2,Current}$, $G_{CF_4,Current}$ and $G_{Voltage,Feeding}$) was 2. The order of volume/feeding (TF) was 2. The highest time delay was computed as 12 s for CO, and the feeding relationship (Eq. (13), and 10 s for the voltage and current relationship (Eq.12). Due to Eqs. 9–16, the value of the coefficient b3 is zero or represents a small value in some cases. This implies that the poles related to the TFs ($G_{CO,Current}$, $G_{CF_4,Current}$, $G_{Voltage,Current}$, $G_{CO,Feeding}$, $G_{CO_2,Feeding}$, and $G_{CF_4,Feeding}$) can be assigned to zero. However, the other TFs ($G_{CO_2,Current}$ and $G_{Voltage,Feeding}$) have complex poles that cause oscillations in the outputs. The model for each output was obtained using these transfer function models.

3.1.2. Auto-Regressive with Extra inputs (ARX) model

The Auto-Regressive with Extra inputs (ARX) model can be represented by two vectors, referred to as the input regression vector $u(t)$ and
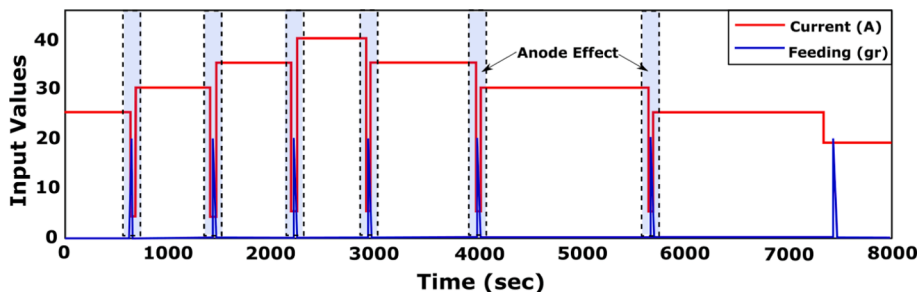

Fig. 3. Input data set including current and feeding for the Molten Salt Electrolysis process along with the representation of the regions where the anode effect occurs.
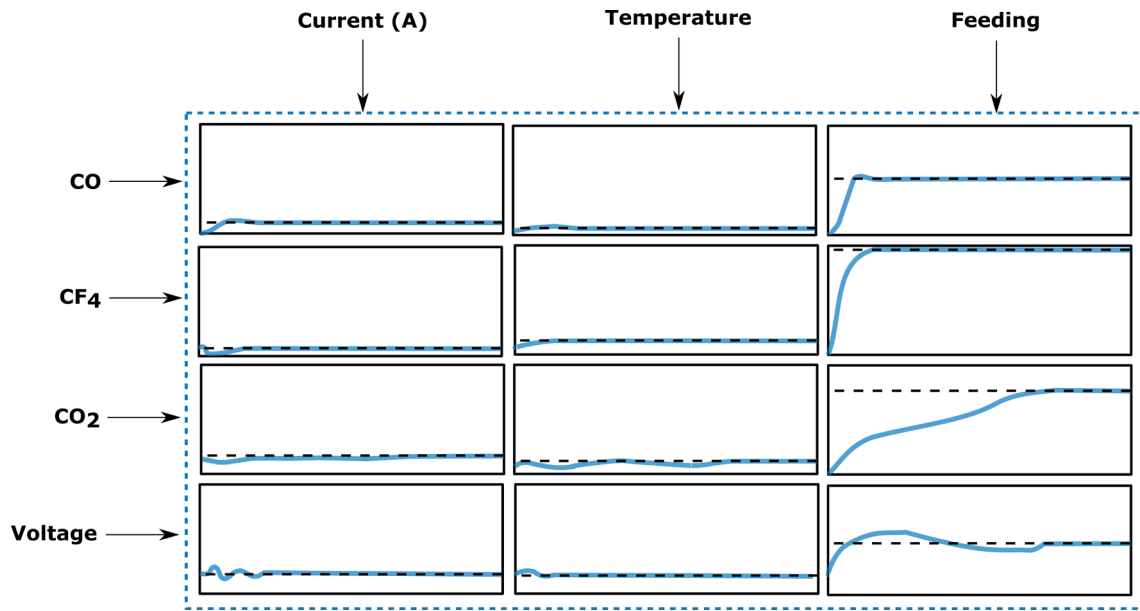
Fig. 4. The step response of the outputs (CO, CF$_4$, CO$_2$, and Voltage) related to inputs (Current, Temperature, and Feeding).

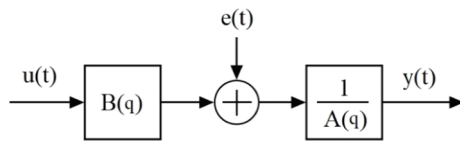**Fig. 5.** ARX model structure with input (u(t)), output (y(t)) and error (e(t)) [19].

the output regression vector $y(t)$. The structure of the ARX model is illustrated in Fig. 5.

where white Gaussian noise is represented by $e(t)$ and $A(q)$ and $B(q)$ are the output and input of the polynomial matrices, respectively.

The ARX model [19] can be formalised as Eq. (17).

$$A(q)y(t) = B(q)u(t - n_k) + e(t) \quad (17)$$

where n_k denotes the system delay. The input–output polynomial matrices ($A(q)$ and $B(q)$) [19] can be represented by Eqs. (18).

$$\begin{cases} A(z) = 1 + a_1 z^1 + \cdots + a_{n_a} z^{-n_a} \\ B(z) = b_1 + b_2 z^{-1} + \cdots + a_{n_b} z^{-n_b} \end{cases} \quad (18)$$

where a_{nb} and n_b represent the orders of the output and input polynomials, respectively. The $[a_1 \ldots a_{na} b_1 \ldots a_{nb}]$ are unknown coefficients of the ARX model that must be identified using the LSE method. A suitable ARX model was developed using prior knowledge and trial-and-error approach. Finally, the orders of n_a, n_b, and n_k were chosen, as represented in Eq. (19):

$$na = \begin{bmatrix} 2 & 1 & 7 & 11 \\ 2 & 0 & 2 & 2 \\ 1 & 0 & 3 & 0 \\ 6 & 1 & 1 & 1 \end{bmatrix}, \quad nb = \begin{bmatrix} 4 & 1 \\ 7 & 9 \\ 1 & 1 \\ 1 & 1 \end{bmatrix}, \quad nk = \begin{bmatrix} 0 & 12 \\ 3 & 1 \\ 8 & 2 \\ 10 & 1 \end{bmatrix} \quad (19)$$

The developed discrete-time ARX model for multi-input multi-output (MIMO) systems [20] is represented by Eq. (20).

$$y(t) + a_1 y(t-1) + \ldots + a_{na} y(t-na) = b_1 u(t-nk) + \ldots + b_{nb} u(t-nb-nk+1) + e(t) \quad (20)$$

The coefficients identified in the ARX model are listed in Table 1.

Table 1
Identified coefficients of the ARX model.

Output	Polynomial	The Identified Coefficients
CO	$A(q)$	[1–1.818 0.833]
	$A_2(q)$	[−3.581]
	$A_3(q)$	[−3832 4235–426.7–336.2 243.6–32.8 56.4]
	$A_4(q)$	[3.5–7.6 5.0–0.2–4.1 30.8–26.7 7.1–9.5 7.4 3.468]
	$B_1(q)$	[25.8–12.39 3.398 3.723]
	$B_2(q)$	[0 0 0 0 0 0 0 0 0 0 19.54]
CO$_2$	$A(q)$	[1–1.839 1.301–0.4526]
	$A_1(q)$	[2.152e-06]
	$B_1(q)$	[0 0 0 0 0 0 0 0.003]
	$B_2(q)$	[0–0.0004]
CF$_4$	$A_1(q)$	[0.0001–0.0001]
	$A_3(q)$	[0.8–2.5]
	$A_4(q)$	[0.025–0.07]
	$B_1(q)$	[0 0–0.06 0.02 0.001 0.06–0.03–0.006 0.03]
	$B_2(q)$	[0.2 0.06 0.2 0.08 0.2 0.1 0.2 0.0015 0.1]
Voltage (V)	$A(q)$	[1–0.7]
	$A_1(q)$	[−0.003 0.005–0.001–8.8e-05–0.001 8.3e-05]
	$A_2(q)$	[−0.1867]
	$A_3(q)$	[−0.195]
	$B_1(q)$	[0 0 0 0 0 0 0 0 0–0.004]
	$B_2(q)$	[0.0381]

3.1.3. Hammerstein-Weiner (HW) model

Because the linear model is only sufficient to obtain simple linear relations, it becomes insufficient for systems with nonlinear behaviours. On the other hand, the Hammerstein-Weiner model makes it possible to recognise the nonlinearities of both the inputs and outputs. The HW model has been applied in several areas such as modelling electromechanical systems and controlling chemical processes. These processes have nonlinear relationships between output and input. The HW models contain both linear and nonlinear blocks. The blocks of the HW model for each variable are connected in series. The structure of the HW model is illustrated in Fig. 6.
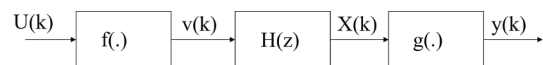

Fig. 6. Structure of the Hammerstein-Wiener (HW) model with input (U(k)) and output (y(k)) [22].

where U(k) is the input variable and f is a nonlinear function that transforms the input data $U(k)$ into $v(k)$. $v(k)$ is an internal variable of the linear function. $H(z)$ is a linear TF model that transforms $v(k)$ into $X(k)$. $X(k)$ is another internal variable for the nonlinear output block. $H(z)$ can be described in a manner similar to a linear dynamic model (TF). Recognising the nonlinearity of the inputs, the Hammerstein model is applied according to Eq. (21).

$$v(k) = f(U(k)) \qquad (21)$$

Then, Eq. (22) was used to obtain the dynamic responses of the variables.

$$X(k) = H(z)v(k) \qquad (22)$$

The approximate response was computed with the nonlinearities of the output using the Weiner model according to Eq. (23).

$$y(k) = g(X(k)) \qquad (23)$$

Input nonlinearity can be computed using a static (memoryless) function, where the output value depends only on the input value. The input nonlinearity function can be configured as a wavelet network. Here, the output nonlinearity is also a static function, similar to input nonlinearity. Moreover, the output nonlinearity can be configured similarly to the input nonlinearity.

3.2. Artificial Neural network

In this study, an Artificial Neural Network (ANN) was used to obtain a time-variant model of the Molten Salt Electrolysis process. There are three general steps for modelling the process. First, the process variables, which include the measurement and control variables, must be described as either input or output. The outgases (CO, CO_2, and CF_4) and

voltage values were defined as the outputs of the model, whereas the feeding material, current value, time, and previous output data were used as the model inputs. It is noteworthy that the data were divided into training, evaluation, and test data, representing 70 %, 10 %, and 20 %, respectively. Another significant issue is that the parameters of the ANN model, which are the number of neurones, hidden layer, type of activation function, and optimiser, were obtained for the best model. The structure of the proposed ANN model is illustrated in Fig. 7.

Several neural structures were compared in terms of their fitting accuracy to create a proper model. All parameters and their effects on the ANN performance are listed in Table 2.

The best model is obtained for our process with eight inputs, 16 neurones, seven hidden layers, a rectified linear unit (ReLU) in the output layer, and Adam as the optimiser. The average Mean Square Error values (MSE) for the training and validation were computed as 0.00865 and 0.0932, respectively.

4. Results and discussion

System identification models and Artificial Neural Network models for the Molten Salt Electrolysis process were examined to compare their performances on outgas models such as CO, CO_2, CF_4, and voltage values. Satisfactory results were obtained based on the output pattern. Furthermore, dynamic and deep neural network (DNN) models were implemented for CO gas emission modelling, which is a relevant output parameter for evaluating the Molten Salt Electrolysis process. The results of the behaviour of the models for CO gas emissions are shown in Fig. 8.

As illustrated in Fig. 8, all models were able to track the pattern of CO gas emissions to some extent. However, the DNN model outperformed the other models, achieving the most accurate results overall. Although
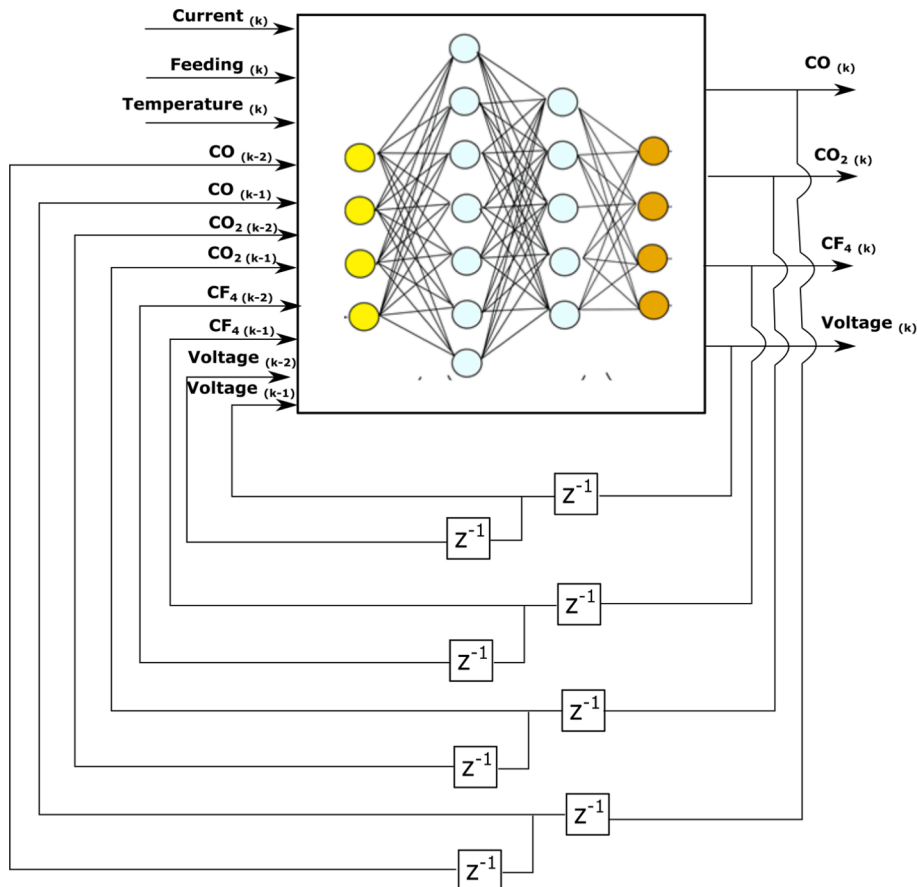

Fig. 7. Structure of the proposed ANN model for the Molten Salt Electrolysis process.

Table 2

ANN configurations for the best model of the Molten salt electrolysis process that shows how the hyperparameters affect the performance.

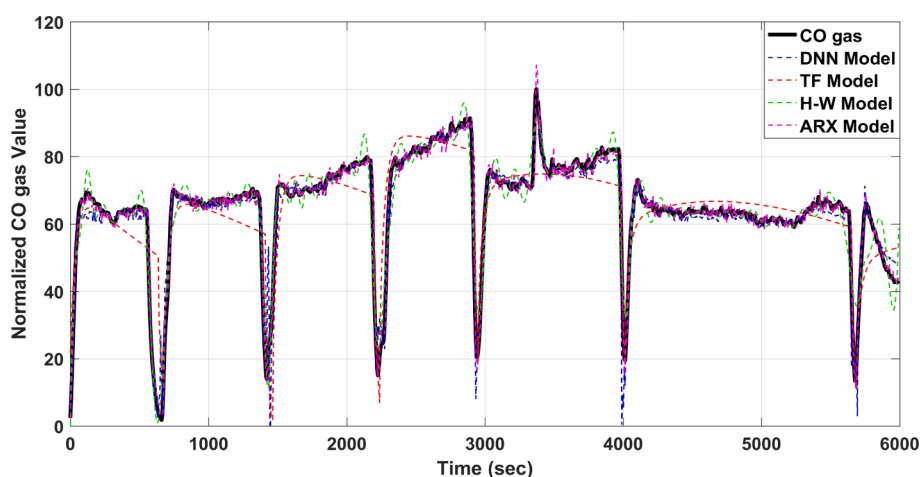| NN Model	Inputs	Neurons	Hidden layers	Act Fcn	Training methods	MSE		Time per epoch (s)
						Train	Val	
Models	8	4–28	1–15	Sigmoid, tanh, relu, leakyrelu relu	Rmsprop, adam, sgd, adadelta adam	0.00865–0.7665	0.0932–0.9876	13–175
Best Model	8	16	7			0.00865	0.0932	17

Fig. 8. measured and modelled CO gas emissions as an output of the Molten Salt Electrolysis.

the ARX model was able to produce satisfactory results, the TF and Hammerstein-Weiner (HW) models showed limitations in terms of accurately predicting the CO gas levels. Furthermore, when anode effects occurred during the process, all models exhibited unpredictable behavior, indicating a need for further investigation and refinement in future studies.

For the integrity of the process, CO_2 is another important gas that represents the current state of the Molten Salt Electrolysis process. The measured data and the model results for CO_2 gas emissions are shown in Fig. 9.

Similar to the CO gas results, all the models succeeded in following the basic pattern of CO_2 gas emissions. However, the DNN and the estimated ARX models override the TF and HW models in terms of their exact values.

In the case of insufficient metal oxides, the system becomes unstable owing to the anode effect. This results in gas bubbles around the anode electrode, the formation of CF_4, and abnormal voltage behaviour

applied to the electrolytic cell. Therefore, the prediction of the anode effect can be addressed by modelling the formation of CF_4 and voltage. The results obtained for the CF_4 gas model are shown in Fig. 10.

Fig. 10 shows that the modelled CF_4 gas values partially matched the real experimental data. Specifically, the DNN and ARX models exhibited fewer errors in predicting the exact values of the CF_4 gas. It is worth noting that the CF_4 gas was generated simultaneously with the occurrence of anode effects in the cell, which was typically accompanied by abnormal changes in the voltage values. Therefore, tracking the changes in voltage values may provide additional support for detecting the anode effect. Fig. 11 illustrates the corresponding voltage measurements and modelled results, demonstrating the correlation between voltage changes and CF_4 gas emissions.

In Fig. 11, there are two different behaviours of the voltage value. These are described as cases with and without the anode effects. Without the Anode effect, the voltage exhibited an almost stable behaviour. The proposed model could fit the actual voltage values. The fitting ratio was
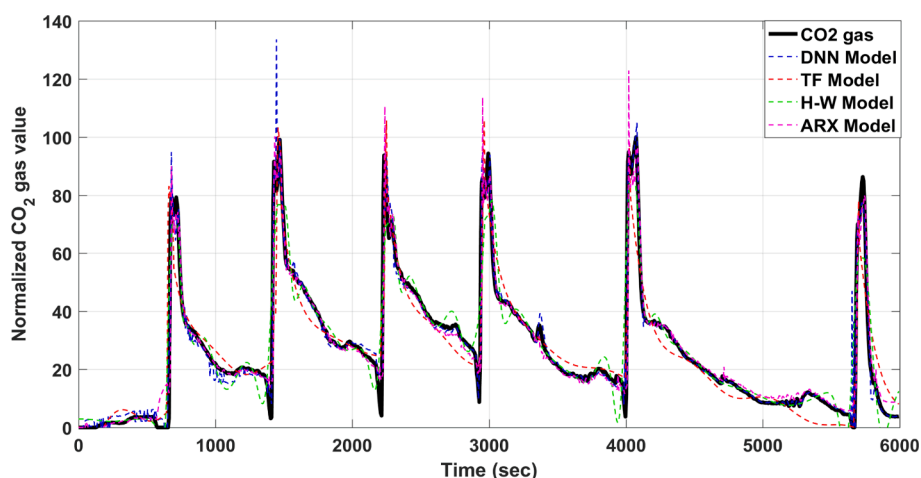
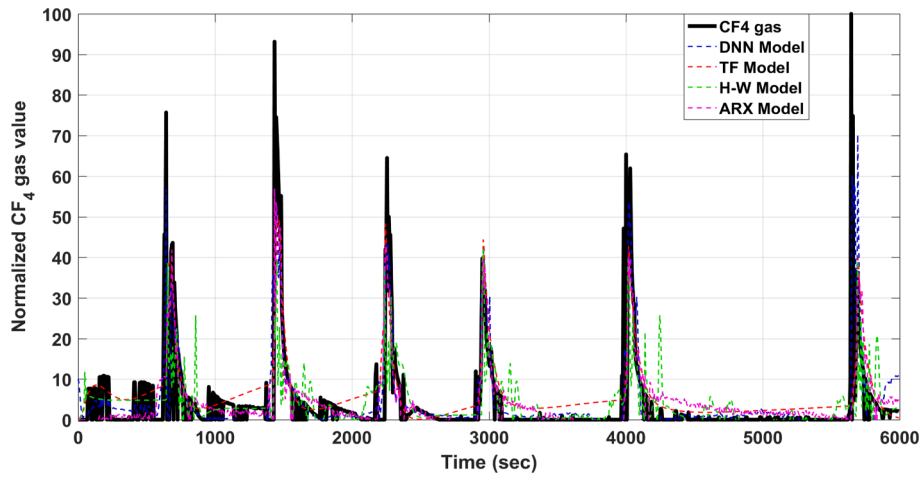**Fig. 9.** measured and modelled CO_2 gas emissions as one of the outputs of the Molten Salt Electrolysis.

Fig. 10. measured and modelled CF$_4$ gas emissions as one of the outputs of the Molten Salt Electrolysis.
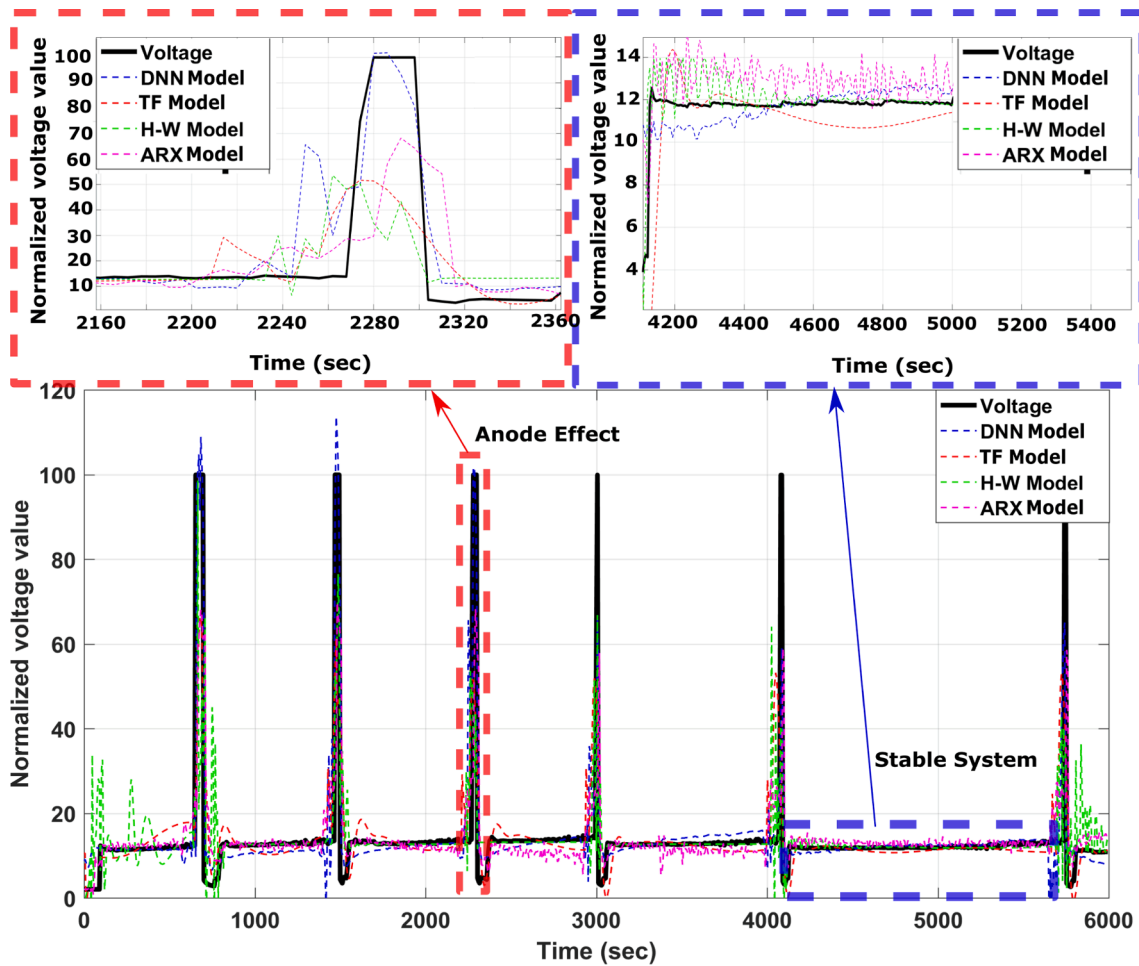

Fig. 11. The proposed "models" result in estimating the voltage value as one of the outputs of the Molten Salt Electrolysis.

higher than that of the anode effect. To display the anode effect on the proposed models, the errors of the DNN and ARX models with the highest accuracy are shown in Fig. 12.

As shown in Fig. 12, the model accuracy decreased because of the anode effect. When the Anode effect occurs in the cell, its initial effects can be recognised using the previous changes in the voltage value. However, the suggested models fail to estimate the exact value of the anode effect. The latter can affect the average error of the model. The

obtained Mean Square Error (MSE) error values for each output parameter and the corresponding standard deviation (σ) are given in Tables 3 and 4 according to the existence of the anode effect in the process.

As shown in Tables 3 and 4, the performance of the proposed model was better when the anode effect did not occur in the cell. Nonetheless, all models allow the basic pattern of outputs to be followed. The results showed that the DNN model had the highest accuracy and least deviation for each output parameter regardless of the anode effect.
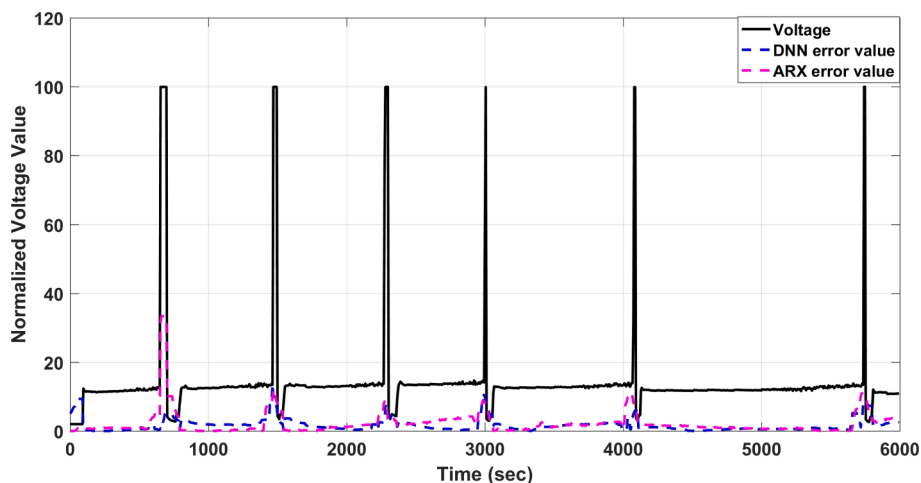
Fig. 12. The errors of the DNN and the ARX models for voltage estimation as one of the outputs of the Molten Salt Electrolysis.

Table 3
Results of the Mean Square Error (MSE) and standard deviation for the models with the anode effect.

Output	TF Model		HW Model		ARX Model		DNN Model	
	MSE	σ	MSE	σ	MSE	σ	MSE	σ
CO	0.0889	±0.19	0.0468	±0.059	0.0442	±0.051	0.0441	±0.0216
CO_2	0.0754	±0.179	0.3662	±0.071	0.0610	±0.0629	0.0409	±0.0192
CF_4	0.0918	±0.163	0.0916	±0.088	0.0666	±0.0817	0.0601	±0.0413
Voltage	0.1077	±0.201	0.1143	±0.1002	0.1124	±0.0992	0.0741	±0.0392

Table 4
Results of the Mean Square Error (MSE) and standard deviation for models without the anode effect.

Output	TF Model		HW Model		ARX Model		DNN Model	
	MSE	σ	MSE	σ	MSE	σ	MSE	σ
CO	0.0844	±0.17	0.0425	±0.0502	0.0433	±0.0500	0.0425	±0.0125
CO_2	0.0798	±0.11	0.3402	±0.0711	0.0729	±0.0700	0.0423	±0.0171
CF_4	0.0907	±0.107	0.0910	±0.0810	0.0582	±0.0900	0.0731	±0.0209
Voltage	0.1045	±0.168	0.1091	±0.0600	0.1098	±0.0869	0.0775	±0.0199

5. Conclusion

In this study, system identification and artificial intelligence (AI) models were developed for Molten Salt Electrolysis. The Molten Salt Electrolysis Process can be described as a nonlinear electrochemical process that experiences anode passivation owing to the lack of oxides in the electrolyte, leading to the formation of toxic and undesired gases and inhibition of current flow. This passivation state is known as the anode effect. The following methods were used to model the Molten Salt Electrolysis process with and without the anode effect. System identification methods, including linear, nonlinear, and data-based models, were used to obtain the entire process behaviour. For this purpose, a TF estimation method is first implemented. Using this method, linear relationships between the inputs and outputs were obtained. The results indicated that the TF model was insufficient for interpreting nonlinear changes such as the physical parameters of the anode effect. However, it provides approximate results and can be implemented easily. Second, the Hammerstein-Wiener (HW) model was implemented for the nonlinearity of the process. The model used wavelet transformations for the nonlinear parts of the inputs and outputs as well as dynamic linear relations. The HW model can be used as a gray-box model after determining the dynamic relationship of the Molten Salt Electrolysis process. Similar to TF, it can be implemented more easily than black-box models such as deep neural networks (DNN). Third, the ARX model, which is a data-based method, was utilised as another system identification method. This demonstrates a relatively good fitting performance, which is better than that of the TF and HW models, but lower than that of the DNN method. Fourth, a deep neural network was developed to model the Molten Salt Electrolysis process. The DNN models succeeded in predicting the nonlinear processes. The good fitting performance applies to scenarios with and without the anode effect, overcoming the sudden changes in the dynamic parameters of the process. However, its implementation is not as easy as other identification methods such as the TF and HW models. Devices compatible with an NN library are required for the implementation of DNN models. It should also be noted that the DNN may not be as successful as the presented results when real-time data or a new dataset are used. Finally, the results of each model were compared. The DNN model exhibited the highest accuracy. This was achieved by utilising eight neurones, seven hidden layers, and Adam as the optimiser. Given this information, it is recommended that these models be run as parallel tools to estimate the performance of the model process for real-time implementations.

CRediT authorship contribution statement

Ozan Kaya: Methodology, Software, Validation, Formal analysis, Investigation, Writing - Original Draft. **Masoud Abedinifar:** Data Curation, Software, Writing - Original Draft. **Dominic Feldhaus:** Methodology, Investigation, Writing - Original Draft. **Fabian Diaz:** Conceptualization, Writing - Review & Editing, Project administration,

Funding acquisition. **Şeniz Ertuğrul:** Supervision. **Bernd Friedrich:** Supervision. Informed consent was obtained from all participants included in this study.

Declaration of Competing Interest

The authors declare that they have no known competing financial interests or personal relationships that could have appeared to influence the work reported in this paper.

Data availability

I have added the code and data used for the modelling.

Appendix A. Supplementary data

Supplementary data to this article can be found online at https://doi.org/10.1016/j.commatsci.2023.112527.

References

[1] Y. Yang, A. Walton, R. Sheridan, K. Güth, R. Gauß, O. Gutfleisch, B.-M. Steenari, T. Van Gerven, P.T. Jones, et al., REE Recovery from End-of-Life NdFeB Permanent Magnet Scrap: A Critical Review, J. Sustain. Metall. 3 (2017) 122–149.

[2] E.E. Kaya, O. Kaya, S. Stopic, S. Gürmen, B. Friedrich, NdFeB Magnets Recycling Process: An Alternative Method to Produce Mixed Rare Earth Oxide from Scrap NdFeB Magnets, Metals (basel). 11 (2021) 716.

[3] L. Diaz, P. Chamelot, M. Gibilaro, L. Massot, J. Serp, Electrochemical Behavior of Neodym-ium in Molten Chloride Salts, Rare Metal Technol. (2017) 77–86.

[4] P. Taxil, P. Chamelot, L. Massot, C. Hamel, Electrodeposition of alloys or compounds in molten salts and applications, J Min Metall B Metall 39 (2003) 177–200.

[5] Y. Yang, C. Lan, L. Guo, Z. An, Z. Zhao, B. Li, Recovery of rare-earth element from rare-earth permanent magnet waste by electro-refining in molten fluorides, Separation Pu-Rification Technol. 233 (2020), 116030.

[6] C. Huang, X. Liu, Y. Gao, S. Liu, B. Li, Cathodic processes of neodymium(iii) in LiF-NdF3-Nd2O3 melts, Faraday Discuss. 190 (2016) 339–349.

[7] E. Stefanidaki, C. Hasiotis, C. Kontoyannis, Electrodeposition of neodymium from LiF–NdF3–Nd2O3 melts, Electrochim. Acta 46 (2001) 2665–2670.

[8] Z. Chen, et al., Electrochemical deposition of neodymium in LiF-CaF2 from Nd2O3 assisted by AlF3, Electrochim. Acta 261 (2018) 289–295.

[9] X. Guo, Z. Sun, J. Sietsma, B. Blanpain, M. Guo, Y. Yang, Quantitative Study on Dissolution Behavior of Nd2O3 in Fluoride Melts, Ind. Eng. Chem. Res. 57 (2018) 1380–1388.

[10] G.-G. Lee, S.-K. Jo, Lee C-K et al Study on electrolysis for neodymium metal production, Rare Metal Technol. (2015) 249–252.

[11] X. Liu, C. Huang, B. Li, The Effects of NdF2 on Current Efficiency of Nd Extrac-tion from NdF3-LiF-Nd2O3 Melts, Mater. Trans. 58 (2017) 395–399.

[12] R. Thudum, A. Srivastava, S. Nandi, A. Nagaraj, R. Shekhar, Molten salt electrolysis of neodymium, Mineral Process. Extractive Metall. 119 (2013) 88–92.

[13] H. Vogel, B. Friedrich, Reducing greenhouse gas emission from the neodymium oxide electrolysis. Part II: Basics of a process control avoiding PFC emission, Int. J. Nonferrous Metall. 6 (3) (2017) 27–46.

[14] J.R. von Asmuth, M. Knotters, Characterising groundwater dynamics based on a system identification approach, J. Hydrol. 296 (1–4) (2004) 118–134.

[15] A. Simpkins, System identification: Theory for the user, (ljung, l.; 1999)[on the shelf], IEEE Rob. Autom. Mag. 19 (2) (2012) 95–96.

[16] Boussalem, Chahira, et al. "Fractional Order Integral Controller Design Based on a Bode's Ideal Transfer Function: Application to the Control of a Single Tank Process." International Conference on Electrical Engineering and Control Applications. Springer, Singapore, 2019.

[17] E.A. Dil, M. Ghaedi, A. Asfaram, The performance of nanorods material as adsorbent for removal of azo dyes and heavy metal ions: application of ultrasound wave, optimisation and modeling, Ultrasonics Sonochem. 34 (2017) 792–802.

[18] C. Sankar Rao, M. Chidambaram, Subspace identification of transfer function models for an unstable bioreactor, Chem. Eng. Commun. 202 (10) (2015) 1296–1303.

[19] F. Piltan, S. TayebiHaghighi, N.B. Sulaiman, Comparative study between ARX and ARMAX system identification, Int. J. Intell. Syst. Appl. (IJISA) 9 (2) (2017) 25–34.

[20] B. Restrepo, D. Tucker, L.E. Banta, Recursive system identification and simulation of model predictive control based on experimental data to control the cathode side parameters of the hybrid fuel cell/gas turbine, J. Electrochem. Energy Convers. Storage 14 (2017) 3.

[21] R. Haddouche, B. Chetate, M.S. Boumedine, Neural network ARX model for gas conditioning tower, Int. J. Model. Simul. 39 (3) (2019) 166–177.

[22] L. Esmaeilani, J. Ghaisari, M.A. Bagherzadeh, Bayesian approach to identify Hammerstein-Wiener nonlinear model in presence of noise and disturbance, IET Control Theory Appl. 13 (3) (2019) 367–376.

[23] P. Abinayadhevi, S.J. Suji Prasad, Identification of pH process using Hammerstein-Wiener model, 2015 IEEE 9th international conference on intelligent systems and control (ISCO). IEEE, 2015.

[24] M.Y. Abdollahzadeh Jamalabadi, Impedance spectroscopy study and system identification of a solid-oxide fuel cell stack with Hammerstein-Wiener model, J. Electrochem. Energy Convers. Storage 14 (2017) 3.

[25] M. Hadjiski, I. Kalaykov, Neural network modelling and control of parameter depending metallurgical plants, IFAC Proceedings Volumes 31 (23) (1998) 375–380.

[26] H.T. Su, T.J. McAvoy, Identification of chemical processes using recurrent networks, in: 1991 American Control Conference, IEEE, 1991, June, pp. 2314-2319.

[27] O. Nerrand, P. Roussel-Ragot, D. Urbani, L. Personnaz, G. Dreyfus, Training recurrent neural networks: Why and how? An illustration in dynamical process modeling, IEEE Trans. Neural Netw. 5 (2) (1994) 178–184.

[28] S.N. Kumpati, P. Kannan, Identification and control of dynamical systems using neural networks, IEEE Trans. Neural Netw. 1 (1) (1990) 4–27.

[29] D. Haesloop, B.R. Holt, A neural network structure for system identification. In 1990 American Control Conference, IEEE, 1990, May, pp. 2460-2465.

[30] B.J. Kim, Applying Modified Backpropagation Algorithm to Chemical Reaction System, Int. J. Hybrid Inform. Technol. 9 (9) (2016) 13–22.

[31] M.A. Serio, Y. Chen, M.A. Wójtowicz, E. Suuberg, July). Pyrolysis processing for solid waste resource recovery in space. In Proceedings of 30th International Conference on Environmental Systems, 2000.

[32] G.O. Tirian, I. Filip, G. Proştean, Adaptive control system for continuous steel casting based on neural networks and fuzzy logic, Neurocomputing 125 (2014) 236–245.

[33] V.S. Cvetković, D. Feldhaus, N.M. Vukićević, T.S. Barudžija, B. Friedrich, J. N. Jovićević, Investigation on tof electrochemical behabehavior deposition mechanism of neodymium in NdF3–LiF–Nd2O3 melt on Mo electrode, Metals 10 (5) (2020) 576.

[34] V.S. Cvetković, N. Vukićević, D. Feldhaus, T. Barudžija, J. Stevanović, B. Friedrich, J.J. Jovićević, Study of Nd deposition onto W and Mo cathodes from the molten oxide-fluoride electrolyte, Int. J. Electrochem. Sci. 15 (7) (2020) 7039–7052.

[35] E. Morrice, R.G. Reddy, Solubility of rare earth oxides in fluoride melts, in: In Symposium on High Temperature and Materials Chemistry, 1989, p. 31.

[36] X. Guo, J. Sietsma, Y. Yang, Solubility of rare earth oxides in molten fluorides. ERES2014 (2014) 149-155.

[37] K.-R. Liu, J.-S. Chen, X.-J. Wei, Anode critical current density of neodymium electrolysis in fluoride system, Chinese J. Nonferrous Metals 11 (2001) 99–101.

[38] H. Vogel, B. Flerus, F. Stoffner, B. Friedrich, Reducing greenhouse gas emission from the neodymium oxide electrolysis. Part I: analysis of the anodic gas formation, J. Sustainable Metall. 3 (1) (2017) 99–107.

[39] V.S. Cvetković, D. Feldhaus, N.M. Vukićević, T.S. Barudžija, B. Friedrich, J. N. Jovićević, Electrochemical study of Nd and Pr co-deposition onto Mo and W from molten oxyfluorides, Metals 11 (9) (2021) 1494.

[40] M. Iffert, R. Ganther, J. Opgen-Rhein, Reduction of greenhouse gases from electrolysis, Die Reduktion von Treibhausgasen in der Elektrolyse, Erzmetall, 2002, p. 55.

[41] R. Keller, K.T. Larimer, Anode effect in Neodymium oixde electrolysis, J. Minerals, Metals Mater. Soc. (1997).